Atmospheric Research 169 (2016) 331–339

Contents lists available at ScienceDirect

Atmospheric Research

journal homepage: www.elsevier.com/locate/atmos

Cloud-scale simulation study on the evolution of latent heat processes of mesoscale convective system accompanying heavy rainfall: The Hainan case

Jiangnan Li [a,*], Kailu Wu [a,b], Fangzhou Li [a], Youlong Chen [c], Yanbin Huang [c]

[a] Department of Atmospheric Sciences, School of Environmental Science and Engineering, Sun Yat-Sen University, Guangzhou 510275, PR China
[b] Foshan Meteorological Service, Foshan 528000, PR China
[c] Hainan Meteorological Service, Haikou 570203, PR China

ARTICLE INFO

Article history:
Received 22 June 2015
Received in revised form 2 October 2015
Accepted 18 October 2015
Available online 24 October 2015

Keywords:
MCS
Microphysical process
Latent heat budget
Neighborhood methods

ABSTRACT

This paper investigates the structure of latent heat budgets and dynamical structure of mesoscale convective systems (MCS) accompanying heavy rain using a cloud-scale model WRF simulation for the Hainan case. Results show that: (1) according to the fractions skill score and HK scores, the WDM6 scheme is more suitable to predict the rainfall than other microphysical schemes. (2) During the lifetime of MCSs, the top two heating microphysical processes are water vapor condensed into cloud water and water vapor condensed into rainwater. The total latent heat is closely related to the top two heating processes. However, the change of latent heat released by some microphysical processes is not identical with the different rainfall processes. (3) The total latent heat of MCS1 increases during the short life, while the total latent heat of MCS2 and MCS3 reach maximum during the mature stage. The difference is mainly caused by the latent heat of water vapor condensed into cloud water and rainwater. The total latent heat released by cond and rcond of MCS1 is smallest during the mature stage, while it is largest during the mature stage of MCS2 and MCS3. (4) The vertical motions are different with different MCSs. The descending motion of the short-lived process (MCS1) is strongest during the mature stage. It caused the smallest latent heat released by water vapor condensed into cloud water and rainwater at the same period. Besides, there are some differences in the change of latent heat released by microphysical processes of MCS2 and MCS3, which are closely related to the drag force of the vertical motion.

1. Introduction

Heavy rainfall is one of the main types of natural weather conditions in Southern China. Heavy rainfall frequently results from mesoscale convective systems (MCSs) that accompany monsoon fronts and typhoons. An MCS occasionally brings sudden and excessive amounts of precipitation locally, thus causing loss of lives and extensive damage to properties. MCS frequently occurs in South China, East China and Huang-Huai River valley (Wang and Cui, 2011, 2012; Meng et al., 2003, 2005; Zheng et al., 2013; Wang et al., 2014). Fundamental details about MCS can be found in the work of Houze (1993). To better investigate the various characteristics of MCS, high-resolution observational data such as remote-sensing Doppler radar data are used (e.g., Kim and Lee, 2006; Park and Lee, 2009) and high-resolution numerical experiments are conducted (e.g., Lin et al., 2005; Parker, 2007; Lauwaet et al., 2009; Peters and Schumacher, 2015). Several numerical studies have demonstrated that MCS is difficult to simulate in real cases because initial and boundary data are not sufficiently enforced to identify storms. Therefore, many studies have suggested that data assimilation is a useful tool to improve initial simulation conditions (e.g., Chang et al., 2008; Takuya et al., 2014; Hou et al., 2015).

Microphysical processes affect the dynamical structure and thermodynamic process of MCS (e.g., Li et al., 2002; Wang and Yang, 2003; Lou et al., 2003; Fu and Guo, 2006; Gao et al., 2006; Wang et al., 2009; Li et al., 2013a,b). Adams-Selin et al. (2013) measured the sensitivity of five parameters that are important to operational forecasters to graupel properties: timing of bowing development, system speed, wind gusts, system areal coverage and accumulated precipitation. The significant differences in bow-echo characteristics produced by graupel property variations in convective-resolving models emphasize careful microphysical parameterization design. Huang and Cui (2015) studied the dominant cloud microphysical processes of torrential rainfall. They found that the orders of magnitudes of the various hydrometers and sinks in the strong precipitation period were larger than those in the weak precipitation period, causing a difference in the intensity of precipitation. The latent heat released by microphysical processes has an effect on the development and evolvement process of the mesoscale convective system and it changes the conformation of the cloud system, its movement and the intensity and the distribution of the convective

* Corresponding author.
E-mail address: essljn@mail.sysu.edu.cn (J. Li).

http://dx.doi.org/10.1016/j.atmosres.2015.10.014
0169-8095/

cloud clusters (Tao et al., 2012). The cooling effect of latent heat (evaporation, melting and sublimation) affect the mesoscale downdraft (Fujita, 1959; Brown, 1979), and the heating effect of latent heat (condensation, freezing and desublimation) strengthen the convective motion (Sun and Tan, 2001; Xu et al., 2011). The cold outflows caused by surface evaporative cooling of rain steered the MCS to move away from its original place (Zhao, 2015). Despite considerable progress, a considerable amount of information remains unknown on the cloud microphysical processes of MCS and the structure of the latent heat budget. These related works lacked quantitative calculations and detailed analyses of cloud microphysical processes and associated heat budgets in MCS.

The primary objective of this study was to investigate the differences among latent heat processes in different MCS stages. The weather research and forecasting (WRF) model is used to conduct simulation experiments for the Hainan case. Every associated latent heat budget is calculated, and the results focus on cloud microphysical process and the structure of latent heat budgets at different MCS stages.

This paper is organized as follows. Section 2 presents the description of the MCS case and relative synoptic environment. Section 3 summarizes the model and design of the experiment. Section 4 is a verification of the simulation results. Section 5 is the evolution of the MCSs. Section 6 investigates characteristics of latent heat budgets in different MCS stages. Section 7 shows the vertical profiles of latent heat. Finally, Section 8 is a summary of our findings.

2. Case description

Rainfall lasting 9 days from the night of September 30, 2010 to October 9, 2010 was the longest process in Hainan Island since 1961. From September 30th to October 2nd, the heavy rainfall began. Large and heavy rains occurred in Wanning, Sanya, Baoting and Lingshui. On October 3rd, the heavy rainfalls occurred in most areas of Hainan Island. On October 4th, the rainfall continued to increase. Because of the tropical disturbance strengthening into tropical depression by October 5th, the rainfall peaked. According to the records of automatic weather stations, the maximum accumulated precipitation amount from 0000 UTC to 2400 UTC on 5 October was 881.80 mm in Qionghai Chaoyang hydrological station. On October 6th, the strong rainfall weakened. On October 7th, heavy rainfall occurred again in Haikou. From the 8th to the 9th, Hainan Island continued to experience rainfall. According to preliminary statistics, the direct economic losses stood at 1.131 billion yuan. This paper chose the rainfall which happened from 0000 UTC to 2400 UTC on 5 October to analyze because of the intensity, which is caused by the convergence of southeast low-level jet and east low-level jet accompanying the tropical depression and the cold air from the north.

3. Numerical model and experiment design

The WRF model (V3.4.1) and its 3D-VAR component, i.e., WRF-VAR, are used in the regional forecasting of heavy rainfall events. On a Mercator conformal map, the model is set up with triple two-way interactive nested domains (Fig. 1) with horizontal grid spacing of 27, 9 and 3 km. The model top is at 50 hPa and 37 sigma layers are used in the vertical. The Grell–Devenyi ensemble scheme (Grell and Devenyi, 2002) is used for the two outermost domains (D01 and D02). For the finest domain (D03), no cumulus parameterization scheme (CPS) is used because such schemes are not designed for horizontal and vertical grid spacings smaller than about 5–10 km (Molinari and Dudek, 1992). The following physics model settings are used on all domains: rapid radiative transfer model longwave scheme (Mlawer et al., 1997), Dudhia shortwave scheme (Dudhia, 1989), Noah land-surface model (Chen and Dudhia, 2001), Monin–Obukhov surface layer scheme (Monin and Obukhov, 1954), and the Mellor–Yamada–Janjic planetary boundary layer scheme (Mellor and Yamada, 1982). In this paper, five different microphysical schemes (WDM5, WDM6, WSM6, Lin and Morrison) are used to test the sensitivity of rainstorm simulation. The initial and boundary

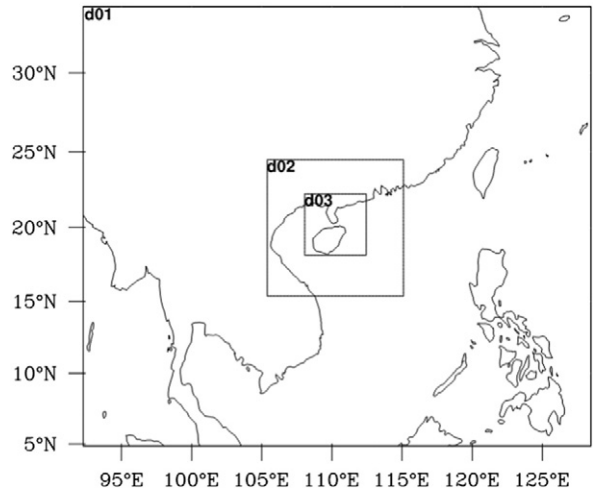

Fig. 1. The experiment domain setting: nested domains for D01, D02 and D03.

conditions are interpolated from the global grid reanalysis data from the National Centers for Environmental Protection/National Center for Atmospheric Research with a 1 × 1 spatial resolution and 6 h temporal resolution. The forecast period is 24 h from 0000 UTC to 2400 UTC on 5 October 2010 with a time step of 150 s. Besides, we utilize the 6-hr "warm start" spin-up from 1800 UTC to 2400 UTC on 4 October. The simulation output has an interval of 30 min. To improve the simulation results, the experiment includes the radar velocity (Vr) and reflectivity (Z) data of the Doppler weather radar in the assimilation at 0000 UTC on 5 October. The design of the control experiment is illustrated in Table 1.

Descriptions of each of the microphysics schemes, its hydrometeor classes and double-moment classes, are provided in Table 2. In this paper, we select the single-moment and double-moment schemes that have six hydrometeor classes. We are also doing some research on the importance of graupel, for simplicity, to make a comparison with the work, we include WDM5 in this paper. The WSM6 (Hong and Lim, 2006; Lin et al., 1983) schemes have some differences in parameters of calculation, while their parameterization processes are similar. The WDM5 and WDM6 schemes (Lim and Hong, 2010) include double-moment rainwater and cloud water distributions, and cloud condensation nuclei (CCN) as a prognostic variable, are different in hydrometeor classes. The WDM5 scheme has no graupel. The Morrison scheme (Morrison et al., 2009) is the most complex scheme used, and has four double-moment classes.

4. Verification of the simulation results

4.1. The neighborhood methods

With the increase of the resolution of model, the traditional verification strategies can't represent the forecast performance well. Recent

Table 1
Designing of the control experiment.

Domain	DOM1	DOM2	DOM3
Horizontal grids	150 × 130	121 × 121	160 × 154
Grid spacing	27 km	9 km	3 km
Integration time	0–24	0–24	0–24
Cumulus parameterization	Grell–Devenyi	Grell–Devenyi	Not used
Microphysics	WSM6	WSM6	WSM6
	WDM5	WDM5	WDM5
	WDM6	WDM6	WDM6
	Lin	Lin	Lin
	Morrison	Morrison	Morrison
Planetary boundary layer	MYJ	MYJ	MYJ

Table 2
Characteristics of the 5 microphysics configurations used in this study.

Microphysics scheme	Hydrometeor classes	Double-moment classes
WSM6	cw, ci, rw, sn, gr	None
WDM5	cw, ci, rw, sn	cw, rw
WDM6	cw, ci, rw, sn, gr	cw, rw
Lin	cw, ci, rw, sn, gr	None
Morrison	cw, ci, rw, sn, gr	rw, ci, sn, gr

Within the classes column, cw, ci, rw, sn and gr represent cloud water, cloud ice, rainwater, snow and graupel, respectively. Mixing ratio is a prognostic value for all classes, and total concentration is the second prognostic value for all double-moment classes.

years have seen the development of spatial verification techniques that include neighborhood methods. They don't require the forecasts to exactly match the observations (Ebert, 2008). Neighborhood methods compute error metrics for the set of all spatial neighborhoods in the domain. They quantify forecast accuracy within spatial windows of different spatial scales around the region of interest. In this paper, two neighborhood verification methods are used.

The first method is the fraction skill score (FSS) (Roberts and Lean, 2008). It compares the forecast and observed precipitation mean values. The score is calculated based on the fraction (1):

$$FSS = 1 - \frac{\frac{1}{N}\sum_N (P_{\text{fcst}} - P_{obs})^2}{\frac{1}{N}\sum_N P_{fcst}^2 + \frac{1}{N}\sum_N P_{obs}^2}, \quad (1)$$

where P_{fcst} and P_{obs} are the fractions of forecast and observed grid points exceeding a certain threshold, and N is the number of neighborhood windows in the domain. The FSS ranges from 0 to 1. A score of 1 represents a perfect forecast and a score of 0 indicates no skill.

The second method is the Hanssen and Kuipers discriminant (HK) (Hanssen and Kuipers, 1965). It measures the accuracy both for events and nonevents. There is a contingency table (Table 3) defined by the combination of different possibilities. The elements of the table are hits, misses, false alarms and correct rejections. The score is calculated by formula (2):

$$\text{HK} = \frac{\text{hits}}{\text{hits} + \text{misses}} - \frac{\text{false alarms}}{\text{false alarms} + \text{correct rejections}} \quad (2)$$

The HK ranges from −1 to 1. An HK score of 1 indicates a perfect forecast both for events and nonevents, while a score of −1 means that hits and correct rejections are zero.

4.2. The fuzzy verification results

Fig. 2 presents the precipitation of the automatic weather stations and the simulated distribution of accumulated rainfall from 0000 UTC to 2400 UTC 5 October 2010 in Hainan Island in DOM3.

The neighborhood verification methods require the model forecast and observation reference to be on the same horizontal grid, so the data of the automatic weather stations were interpolated on the respective model grid. The neighborhood verification scores were determined for increasing neighborhood sizes and various precipitation thresholds. According to the size of DOM3, neighborhood sizes of $s = (1, 3, 5, 9, 17, 33$ and $65)$ grid points were chosen. And for each scale, nine thresholds (1, 10, 25, 50, 100, 200, 400, 600, 800 and 1000 mm) were evaluated according to the accumulated rainfalls of experiments.

Table 3
Contingency table of possible events for a selected threshold.

		Observed	
		Yes	No
Forecast	Yes	Hits	False alarms
	No	Misses	Correct ejections

Table 4 shows the fuzzy verification results from the fractions skill score. The forecast is proportional to the spatial scale, while in inverse proportion to the accumulation threshold. With the WSM6 scheme (the table isn't provided), the forecast is perfect while the threshold is 1 mm. With the thresholds of 10, 25, 50 and 100 mm, the fractions skill scores are above 0.6, which means the rainfall is well predicted. Rainfall at scales of 17, 33 and 65 grids points are predicted except the threshold of 800 and 1000 mm. The maximum score is 0.26 when the threshold is 800 mm. The rainfall exceeding 1000 mm with the WSM6 scheme doesn't match the observation completely. With the WDM6 scheme, the rainfall area (threshold = 1 mm) is predicted successfully. The scores are greater than 0.6 when the thresholds are 10, 25, 50 and 100 mm. When predicting the rainfall exceeding 800 mm, the largest score is 0.52. The scores are −999.0 when the threshold is 1000. In other words, the rainfall of the simulation and the observation don't exceed 1000 mm. With the WDM5 scheme, the rainfall area is also well predicted. However, the scores are almost zero (threshold = 1 mm), and the scores are zero when the threshold is 800. Apparently, the largest rainfall with the WDM5 scheme is about 600 mm. With the LIN scheme, rainfall with a threshold of 1, 10, 25, 50 and 100 mm predicts well. When the thresholds are 200, 400 and 600 mm, the scores can reach more than 0.7. However, it fails to predict the rainfall exceeding 800 mm. Besides, the rainfall exceeding 1000 mm with the LIN scheme doesn't match the observation. It also fails to predict the rainfall exceeding 800 and 1000 mm with the Morrison scheme.

Table 5 shows the fuzzy verification results from the HK scores. With the five microphysical schemes, the rainfalls predict precisely when the threshold is 1 mm and the spatial scale is 65 grid points. With the WSM6 scheme (the table isn't provided), the scores are positive when the thresholds are 10, 25, 50, 100, 200, 400 and 600 mm.

In other words, the hit rate is larger than the false alarm rate. When the threshold is 800 mm, the hit rate is larger with the neighborhood size of 9, 17, 33 and 64. The scores are negative when predicting the rainfall exceeding 1000 mm. It means that the false alarm rate is larger. With the WDM6 scheme, the scores are −999 when the threshold is 1000 mm. That is to say, the largest rainfall with the WDM6 scheme is less than 1000 mm. The simulation's performance is good when predicting rainfall exceeding 800 mm with the spatial scale of 5 grid points or more, and the score can reach 0.89. With the thresholds of 10, 25, 50, 100, 200, 400 and 600, the scores are also positive with the WDM6 scheme. While with the WDM5 scheme, the largest rainfall is less than 800 mm. The rainfall is well predicted when the thresholds are 10, 25, 50 and 100 mm. The false alarm rate is larger when the threshold is 1000 with the Lin and Morrison scheme, while the hit rate is larger while the thresholds are 10, 25, 50, 400, 600 and 800 mm.

According to the fractions skill score, the area with the rainfall exceeding 200 mm is well predicted with the five microphysical schemes. It fails to predict the rainfall exceeding 400 mm with the WDM5 scheme. With the WDM6 and WDM5 scheme, the performances of the rainfall above 600 mm are bad. However, the WDM6 scheme does better than other schemes when predicting the rainfall exceeding 800 mm. The largest rainfalls with the WSM6, Lin and Morrison scheme are above 1000 mm, which are larger than the observations. According to the HK scores, the performance of five schemes were similar when predicting the rainfall exceeding 1 mm, and the hit rates are almost larger than the false alarm rates except when predicting rainfall exceeding 1000 mm. The largest rainfall with the WSM6, Lin and Morrison scheme exceeds 1000 mm, which are not identical with the observation.

Because the simulations are cloud-scale, we also compared the 3 h accumulated rainfall, and the WDM6 scheme does better. Take the accumulated rainfall from 0000 UTC to 0300 UTC, for example, according to the fraction scores and HK scores, the WDM6 and WDM5 schemes are more successful when predicting rainfall between 100 mm and

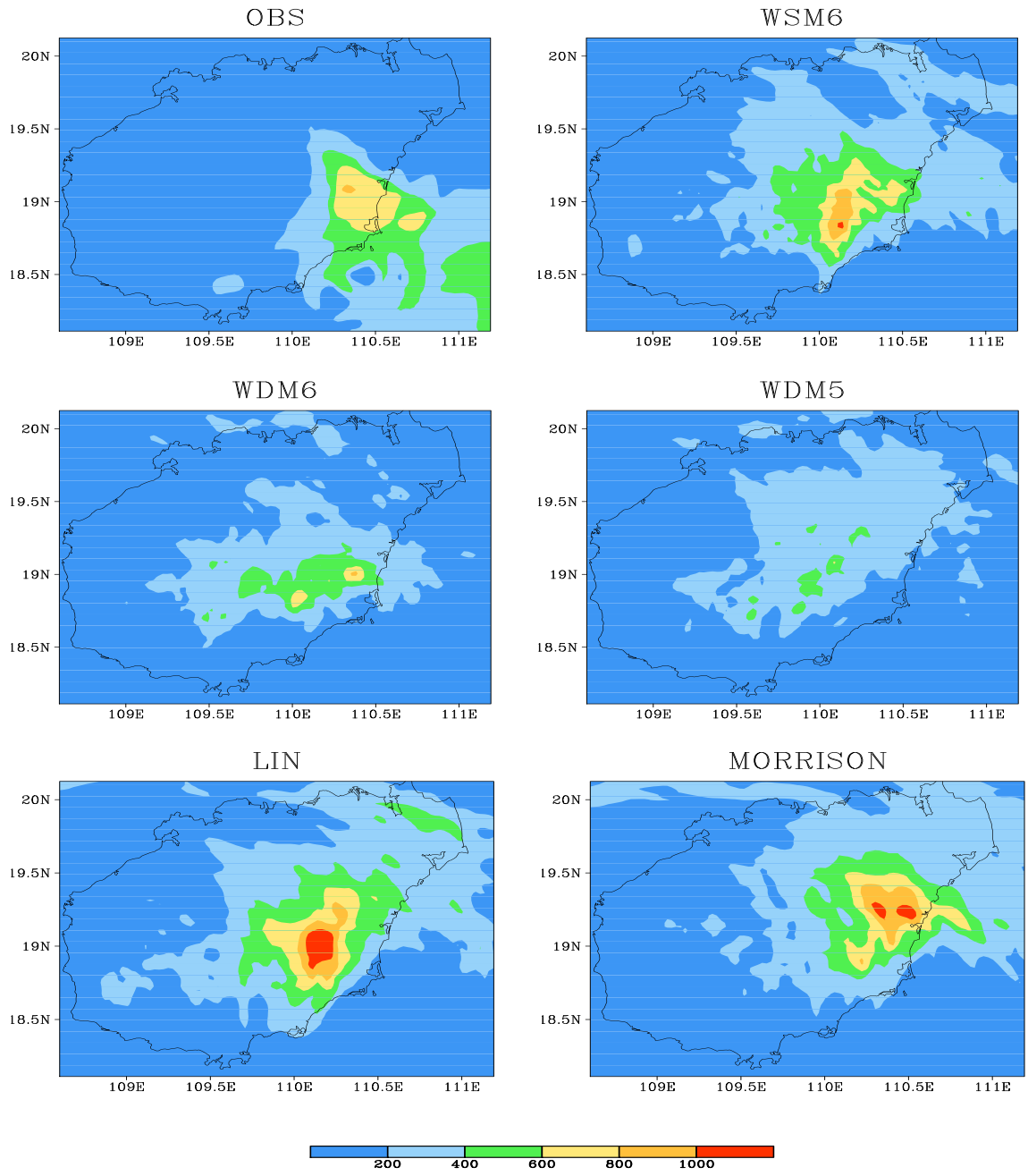

Fig. 2. A total of 24-h accumulated precipitation (unit: mm) from the observation and different schemes.

200 mm, while the Morrison, Lin and WSM6 schemes predict rainfall exceeding 200 mm.

In conclusion, the WDM6 scheme can reproduce the rainfall better. Next, we analyze the characteristics of the rainstorm in Hainan Island with the results of the WDM6 scheme.

5. The evolution of MCSs

Fig. 3 shows the average observation of 1 h accumulated rainfall of the simulated heavy rain area (110.33°E to 110.41°E, 18.96°N to

Table 4
Fractions skill score of WDM6.

Spatial	65	1.00	1.00	1.00	1.00	0.98	0.95	0.80	0.30	0.52	−999.
scale	33	1.00	1.00	1.00	0.99	0.92	0.71	0.63	0.26	0.48	−999.
(pts)	17	1.00	1.00	0.99	0.95	0.82	0.54	0.41	0.20	0.43	−999.
	9	1.00	1.00	0.97	0.90	0.73	0.46	0.31	0.20	0.34	−999.
	5	1.00	1.00	0.96	0.87	0.68	0.41	0.25	0.19	0.18	−999.
	3	1.00	0.99	0.95	0.85	0.65	0.39	0.22	0.17	0.00	−999.
	1	1.00	0.99	0.93	0.83	0.61	0.35	0.19	0.14	0.00	−999.
		1	10	25	50	100	200	400	600	800	1000

Accumulation threshold (mm).

Table 5
The HK scores of WDM6.

Spatial	65	1.00	0.53	0.53	0.38	0.08	0.21	0.38	0.78	0.89	−999.
scale	33	−0.00	0.52	0.49	0.24	0.15	0.19	0.41	0.66	0.71	−999.
(pts)	17	−0.00	0.49	0.43	0.09	0.18	0.26	0.26	0.30	0.57	−999.
	9	−0.00	0.29	0.24	0.20	0.18	0.20	0.17	0.20	0.38	−999.
	5	−0.00	0.53	0.32	0.19	0.16	0.17	0.14	0.14	0.18	−999.
	3	−0.00	0.52	0.30	0.17	0.16	0.16	0.12	0.11	−0.00	−999.
	1	−0.00	0.51	0.26	0.15	0.16	0.16	0.10	0.08	−0.00	−999.
		1	10	25	50	100	200	400	600	800	1000

Accumulation threshold (mm).

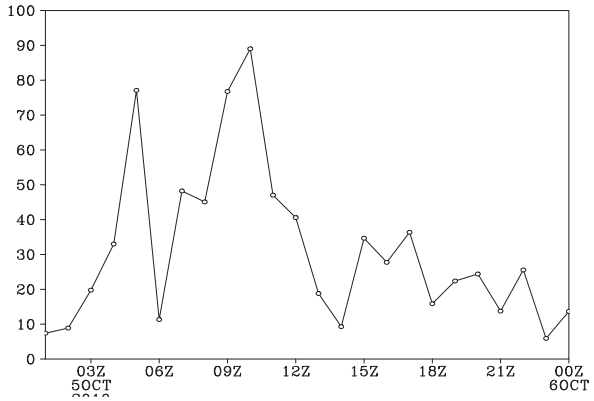

Fig. 3. The observation of 1 h accumulated rainfall (unit: mm).

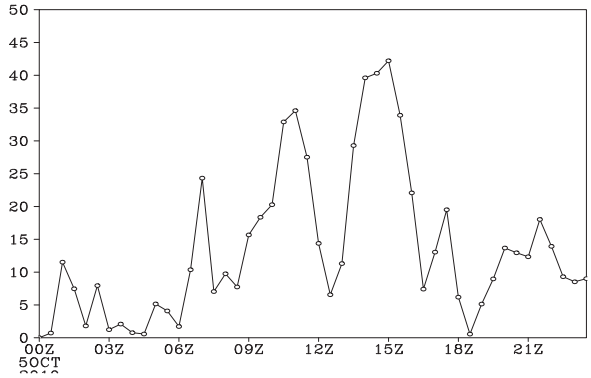

Fig. 4. Half-hour accumulated precipitation of the regional rainstorm (unit: mm) (110.33°E to 110.41°E, 18.96°N to 19.06°N).

19.06°N). Because rainstorm center position of the simulation and the actual observation are not completely equivalent, the observed rainfall intensity (Fig. 3) is somewhat different from the simulation (Fig. 4) every hour. The rainfall from 1400 to 1500 UTC in Fig. 3 is smaller than it in Fig. 4. Actually, the observed rainfall from 1400 to 1500 UTC is heavy in Wenchang, reaching 61.8 mm. Despite this, the observed and simulated rainfall both experience four maximums from 0600 to 1800 UTC. The observed rainfall reaches the max value at 0700 UTC, 1000 UTC, 1500 UTC and 1700 UTC, respectively. The simulated rainfall reaches the peak value at 0700 UTC, 1100 UTC, 1500 UTC and 1700 UTC, respectively.

Fig. 4 shows the average half-hour precipitation of the heavy rain area (110.33°E to 110.41°E, 18.96°N to 19.06°N) where the simulated rainfall exceeds 600 mm in 24 h. We select three generations and disappearance processes to analyze which half-hour accumulated precipitation exceeds 20 mm. The first process (MCS1) is of short duration that lasts from 0600 UTC to 0730 UTC. It develops from 0600 UTC and enters the mature stage at 0630 UTC. Then, the rainfall decreases from 0700 UTC to 0730 UTC. The second process (MCS2) and the third process (MCS3) both last four hours, and the third process is the strongest. They are divided into three stages, respectively: the developing stage (0830 UTC to 1000 UTC, 1230 UTC to 1330 UTC), where accumulated rainfall is moderate; the mature stage, where the rainfall intensity is high (1000 UTC to 1100 UTC, 1330 UTC to 1500 UTC); and the dissipating stage, where rainfall starts to decrease (1100 UTC to 1230 UTC, 1500 UTC to 1630 UTC).

6. Characteristics of latent heat budgets

Phase changes during cloud microphysical conversion processes cause the release of latent heat. However, because of limited observations, we have limited information on the cloud microphysical processes and latent heat budgets of MCS. In this study, we use the parameter output of the WDM6 scheme to calculate and analyze the latent heat budgets. The integrated latent heat release is calculated as follows.

In fraction (3), Q_x is the amount of released latent heat, L is the latent heat of the phase transition, $P_x(i, j, k)$ is the conversion rate of a specific microphysical process averaged over two adjacent model levels, and Δz is the vertical distance between those levels. $\rho(i, j, k)$ is the air density, and Δx and Δy are the horizontal grid spacings.

$$Q_x = \sum_{i,j,k} L \times P_x(i,j,k) \times \rho(i,j,k) \times \Delta x \times \Delta y \times \Delta z \tag{3}$$

In the WDM6 scheme, 26 microphysical processes release latent heat, including 14 processes that release latent heat and 12 processes that absorb latent heat. Tables 6 and 7 show the regional (110.33°E to 110.41°E, 18.96°N to 19.06°N) latent heat release and their contributions during the different stages.

During the first process (0600 UTC to 0730 UTC), the release of total latent heat and the positive latent heat reaches minimum during the mature stage, while the negative latent heat is largest at the same period. During the different stages, the top two heating microphysical processes (in boldface) are water vapor condensed into cloud water (cond) and water vapor condensed into rainwater (rcond). Besides, the top two cooling microphysical processes (in boldface) are the evaporation of rainwater (revp) and melting of graupel (gmlt). Most of the microphysical processes increase from the development stage to the mature stage, and decrease from the mature stage to the dissipation stage except the water vapor condensing into cloud water and rainwater, cloud water collected by snow and graupel, melting of snow and the evaporation of melting snow. The latent heat released by the condensation of water vapor is identical with the change of total latent heat. The latent heat released by cloud water collected by snow and graupel increases with the evolution of the rainfall, while the latent heat released by melting of snow and the evaporation of melting snow decreases.

Table 7 shows the latent heat budget in different stages of MCS2. The total latent heat and the positive latent heat reach a maximum during the mature stage, melting of snow and the evaporation of melting snow, while the negative latent heat increases during the whole time. The top two heating microphysical processes (in boldface) are water vapor condensed into cloud water (cond) and water vapor condensed into rainwater (rcond). During the development stage and the mature stage, the top two cooling microphysical processes (in boldface) are the evaporation of rainwater (revp) and melting of graupel (gmlt). However, during the dissipating stage, the top two cooling processes are the evaporation of rainwater and evaporation of cloud water. There are eight microphysical processes (the deposition of snow and cloud ice, cloud water collected by snow and graupel, rainwater collected by cloud ice, evaporation of the rainwater, the melting of snow and the evaporation of melting snow), which are not identical with the evolution of total latent heat. They have little influence on the increase/decrease of the total latent heat.

Table 8 shows the latent heat budget of MCS3. The total latent heat, the positive latent heat and the negative latent heat increase from the development stage to the mature stage, and decrease from the mature stage to the dissipating stage. The top two heating microphysical processes (in boldface) are water vapor condensed into cloud water (cond) and water vapor condensed into rainwater (rcond). The top two cooling microphysical processes (in boldface) are the evaporation of rainwater (revp) and evaporation of cloud water into water vapor (evap) during the development stage. Differently, during the mature stage and the dissipating stage, the top two cooling microphysical processes (in boldface) are the evaporation of rainwater (revp) and melting of graupel (gmlt). Only the maximum latent heat of two microphysical

Table 6
The latent heat budget in different stages of MCS1.

WDM6	Microphysical processes	Latent heat release value(10^{13} J/h) (the contribution to positive/negative latent heat)					
		Development stage		Mature stage		Dissipating stage	
cond	Water vapor condenses into cloud water	**34.30**	**69.89%**	**28.91**	**62.56%**	**35.50**	**70.20%**
gacr	Rainwater collected by graupel	0.99	2.02%	2.08	4.50%	0.83	1.64%
sdep	Snow deposition growth	1.06	2.16%	1.38	2.99%	1.09	2.16%
idep	Cloud ice deposition growth	3.56	7.25%	3.87	8.37%	3.62	7.16%
gdep	Graupel deposition growth	2.51	5.11%	3.55	7.68%	0.91	1.80%
aacw	Cloud water collected by snow and graupel	0.63	1.28%	0.56	1.21%	0.18	0.36%
sacr	Rainwater collected by snow	0.16	0.33%	0.22	0.48%	0.08	0.16%
igen	Initialization of cloud ice	0.40	0.81%	0.79	1.71%	0.39	0.77%
rcond	Water vapor condenses into rainwater	**5.10**	**10.39%**	**4.41**	**9.54%**	**7.87**	**15.56%**
iacr	Rainwater collected by cloud ice	0.35	0.71%	0.39	0.84%	0.10	0.20%
ihmf	Homogeneous growth of cloud ice	0.00	0.00%	0.00	0.00%	0.00	0.00%
gfrz	Rainwater condenses into graupel	0.01	0.02%	0.03	0.06%	0.00	0.00%
ihtf	Heterogeneous growth of cloud ice	0.01	0.02%	0.02	0.04%	0.00	0.00%
cact	Activation of cloud condensation nuclei	0.00	0.00%	0.00	0.00%	0.00	0.00%
revp	Evaporation of rainwater	**−5.56**	**47.40%**	**−12.37**	**52.28%**	**−4.20**	**53.23%**
cevp	Evaporation of cloud water into water vapor	−1.03	8.78%	−1.07	4.52%	−0.86	10.90%
ssub	Sublimation of snow	−0.08	0.68%	−0.14	0.59%	−0.33	4.18%
gmlt	Melting of graupel	**−3.54**	**30.18%**	**−6.27**	**26.50%**	**−1.43**	**18.12%**
gsub	Sublimation of graupel	−0.02	0.17%	−0.20	0.85%	−0.15	1.90%
gevp	Evaporation of melting graupel	−0.34	2.90%	−1.02	4.31%	−0.41	5.20%
geml	Enhanced melting of graupel	−0.92	7.84%	−2.28	9.64%	−0.20	2.53%
smlt	Melting of snow	−0.03	0.26%	−0.04	0.17%	−0.13	1.65%
isub	Sublimation of cloud ice	−0.20	1.71%	−0.24	1.01%	−0.10	1.27%
sevp	Evaporation of melting snow	−0.01	0.09%	−0.02	0.08%	−0.08	1.01%
seml	Enhanced melting of snow	−0.00	0.00%	−0.01	0.04%	−0.00	0.00%
imlt	Melting of cloud ice	−0.00	0.00%	−0.00	0.00%	−0.00	0.00%
The total positive latent heat		49.08		46.21		50.57	
The total negative latent heat		−11.73		−23.66		−7.89	
The total latent heat		37.35		22.55		42.68	

processes (melting of snow and the evaporation of melting snow) don't occur during the mature stage. These two processes cause a loss of 0.01×10^{13} J/h during the development stage and the mature stage, respectively.

7. The vertical profiles of latent heat

According to the analysis of the preceding context, the total latent heat of MCS1 increases during the short life, while the total latent heat

Table 7
The latent heat budget in different stages of MCS2.

WDM6	Microphysical processes	Latent heat release value(10^{13} J/h) (the contribution to positive/negative latent heat)					
		Development stage		Mature stage		Dissipating stage	
cond	Water vapor condenses into cloud water	**44.35**	**64.37%**	**51.14**	**65.54%**	**36.52**	**70.04%**
gacr	Rainwater collected by graupel	0.50	0.73%	1.04	1.33%	0.20	0.38%
sdep	Snow deposition growth	0.80	1.16%	0.34	0.44%	0.31	0.59%
idep	Cloud ice deposition growth	3.91	5.67%	1.98	2.54%	1.90	3.64%
gdep	Graupel deposition growth	0.48	0.70%	0.65	0.83%	0.23	0.44%
aacw	Cloud water collected by snow and graupel	0.28	0.41%	0.24	0.31%	0.12	0.23%
sacr	Rainwater collected by snow	0.08	0.12%	0.10	0.13%	0.03	0.06%
igen	Initialization of cloud ice	0.05	0.07%	0.09	0.12%	0.05	0.10%
rcond	Water vapor condenses into rainwater	**18.19**	**26.40%**	**22.31**	**28.59%**	**12.62**	**24.20%**
iacr	Rainwater collected by cloud ice	0.26	0.38%	0.14	0.18%	0.16	0.31%
ihmf	Homogeneous growth of cloud ice	0.00	0.00%	0.00	0.00%	0.00	0.00%
gfrz	Rainwater condenses into graupel	0.00	0.00%	0.00	0.00%	0.00	0.00%
ihtf	Heterogeneous growth of cloud ice	0.00	0.00%	0.00	0.00%	0.00	0.00%
cact	Activation of cloud condensation nuclei	0.00	0.00%	0.00	0.00%	0.00	0.00%
revp	Evaporation of rainwater	**−2.55**	**55.80%**	**−3.89**	**54.79%**	**−5.32**	**73.28%**
cevp	Evaporation of cloud water into water vapor	−0.50	10.94%	−0.84	11.83%	**−1.10**	**15.15%**
ssub	Sublimation of snow	−0.05	1.09%	−0.11	1.55%	−0.05	0.69%
gmlt	Melting of graupel	**−0.84**	**18.38%**	**−1.37**	**19.30%**	−0.37	5.10%
gsub	Sublimation of graupel	−0.01	0.22%	−0.04	0.56%	−0.02	0.28%
gevp	Evaporation of melting graupel	−0.08	1.75%	−0.12	1.69%	−0.03	0.41%
geml	Enhanced melting of graupel	−0.13	2.84%	−0.19	2.68%	−0.06	0.83%
smlt	Melting of snow	−0.09	1.97%	−0.03	0.42%	−0.02	0.28%
isub	Sublimation of cloud ice	−0.29	6.35%	−0.50	7.04%	−0.28	3.86%
sevp	Evaporation of melting snow	−0.03	0.66%	−0.01	0.14%	−0.01	0.14%
seml	Enhanced melting of snow	−0.00	0.00%	−0.00	0.00%	−0.00	0.00%
imlt	Melting of cloud ice	−0.00	0.00%	−0.00	0.00%	−0.00	0.00%
The total positive latent heat		68.90		78.03		52.14	
The total negative latent heat		−4.57		−7.10		−7.26	
The total latent heat		64.43		70.93		44.88	

Table 8
The latent heat budget in different stages of MCS3.

WDM6	Microphysical processes	Latent heat release value(10^{13} J/h) (the contribution to positive/negative latent heat)					
		Development stage		Mature stage		Dissipating stage	
cond	Water vapor condenses into cloud water	**58.31**	**66.95%**	**75.46**	**42.30%**	**21.83**	**67.99%**
gacr	Rainwater collected by graupel	0.49	0.56%	8.38	4.70%	0.56	1.74%
sdep	Snow deposition growth	0.33	0.38%	1.38	0.77%	0.42	1.31%
idep	Cloud ice deposition growth	2.07	2.38%	4.24	2.38%	2.37	7.38%
gdep	Graupel deposition growth	0.35	0.40%	3.72	2.09%	0.64	1.99%
aacw	Cloud water collected by snow and graupel	0.27	0.31%	1.36	0.76%	0.22	0.69%
sacr	Rainwater collected by snow	0.09	0.10%	0.75	0.42%	0.11	0.34%
igen	Initialization of cloud ice	0.03	0.03%	0.28	0.16%	0.04	0.12%
rcond	Water vapor condenses into rainwater	**24.76**	**28.43%**	**80.85**	**45.32%**	**5.36**	**16.69%**
iacr	Rainwater collected by cloud ice	0.40	0.46%	1.93	1.08%	0.56	1.74%
ihmf	Homogeneous growth of cloud ice	0.00	0.00%	0.00	0.00%	0.00	0.00%
gfrz	Rainwater condenses into graupel	0.00	0.00%	0.03	0.02%	0.00	0.00%
ihtf	Heterogeneous growth of cloud ice	0.00	0.00%	0.03	0.02%	0.00	0.00%
cact	Activation of cloud condensation nuclei	0.00	0.00%	0.00	0.00%	0.00	0.00%
revp	Evaporation of rainwater	**−3.70**	**66.07%**	**−16.07**	**61.88%**	**−13.28**	**79.47%**
cevp	Evaporation of cloud water into water vapor	**−0.58**	**10.36%**	−0.72	2.77%	−0.56	3.35%
ssub	Sublimation of snow	−0.10	1.79%	−0.15	0.58%	−0.06	0.36%
gmlt	Melting of graupel	−0.45	8.04%	**−4.40**	**16.94%**	**−1.53**	**ss**
gsub	Sublimation of graupel	−0.02	0.36%	−0.09	0.35%	−0.06	0.36%
gevp	Evaporation of melting graupel	−0.05	0.89%	−0.82	3.16%	−0.24	1.44%
geml	Enhanced melting of graupel	−0.16	2.86%	−3.39	13.05%	−0.62	3.71%
smlt	Melting of snow	−0.04	0.71%	−0.03	0.12%	−0.03	0.18%
isub	Sublimation of cloud ice	−0.49	8.75%	−0.28	1.08%	−0.33	1.97%
sevp	Evaporation of melting snow	−0.01	0.18%	−0.01	0.04%	−0.00	0.00%
seml	Enhanced melting of snow	−0.00	0.00%	−0.01	0.04%	−0.00	0.00%
imlt	Melting of cloud ice	−0.00	0.00%	−0.00	0.00%	−0.00	0.00%
The total positive latent heat		87.10		178.41		32.11	
The total negative latent heat		−5.60		−25.97		−16.71	
The total latent heat		81.50		152.44		15.40	

of MCS2 and MCS3 reach their maximum during the mature stage. The difference is mainly caused by the latent heat of water vapor condensed into cloud water and rainwater. Fig. 5 gives the average vertical structure of cond and rcond of MCSs in different periods. The condensation of cloud water of MCS1 is found below 250 hPa. The maximum latent heat released by cond in the mature MCS1 stage reaches 5×10^{13} J/h near 450 hPa, while in the dissipating stage, it exceeds 7×10^{13} J/h near 650 hPa. Below 500 hPa, the latent heat of cond in the mature stage is smallest. The condensation of rainwater in MCS1 appears between 950 hPa and 300 hPa. The maximum latent heat of rcond is found near 550 hPa, and in the dissipating stage it is largest. However, above 450 hPa, the latent heat of rcond is largest in the mature stage. The maxima of MCS2 and MCS2 appear below 600 hPa, and the latent heat released by cond and rcond are largest in the mature stage. The condensation of cloud water of MCS2 exists below 350 hPa, and the condensation of rainwater appears between 950 hPa and 450 hPa. However, the condensation of cloud water of MCS3 is found below 250 hPa, and the condensation of rainwater exists between 950 hPa and 350 hPa.

Because the convective motion of MCS causes the release of large amounts of latent heat, we explain the difference of latent heat between the MCSs through the dynamical structure. Fig. 6 shows the average divergence and vertical velocity of the heavy rain area. From 0600 UTC to 0700 UTC, the convergence area is mainly found between 850 hPa and 400 hPa, and the maximum occurs at 0630 UTC, corresponding to the ascending motion of the middle–high layer and the descending motion of the middle–low layer. The descending motion is more obvious from 0630 UTC to 0700 UTC. During the dissipating stage of MCS1, the convergence area narrows, identical with the diminution of the descending motion. During the life of MCS2, the divergence area is mainly found between 750 hPa and 300 hPa. As a result, the ascending motion mainly occurs below 300 hPa, and reaches its maximum of 2 m/s near 700 hPa, while the descending motion isn't obvious. The convergence and divergence of MCS3 are stronger than MCS2, corresponding to the larger vertical velocity that can reach 4 m/s near 600 hPa, and the ascending motion appears in the high layer. From 1400 UTC to 1630 UTC, the descending motion becomes apparent.

The descending motion of the short-lived process (MCS1) are strongest during the mature stage. On the contrary, the latent heat released by water vapor condensed into cloud water and rainwater are smallest. During the mature stage, the ascending motion of the short-lived process (MCS1) appears in the middle–high level, which corresponds to the largest latent heat released by cond and rcond above 450 hPa. As the air rises, the water vapor condenses. The descending motion is stronger, and the condensation is less. The ascending motion of MCS2 and MCS3 are strongest during the mature stage, and cause the largest latent heat released by the condensation of water vapor. Besides, there are some differences in the change of latent heat released by microphysical processes of MCS2 and MCS3, which are closely related to the drag force of the vertical motion.

8. Conclusions

In this paper, the new-generation mesoscale model WRF is used to conduct simulation experiments for accompanying heavy rain in Hainan Island. After the verification of simulation results, the latent heat budget of microphysical processes and dynamical structure of MCSs have been examined.

According to the fractions skill score and HK scores, the WDM6 scheme is more suitable to predict the rainfall than other microphysical schemes.

During the lifetime of MCSs, the top two heating microphysical processes are water vapor condensed into cloud water and water vapor condensed into rainwater. The most important cooling microphysical process is the evaporation of rainwater. Nevertheless, the total latent heat providing energy to the development of rainfall are closely related with the top two heating processes. However, the change of latent heat released by some microphysical processes are not identical with the different rainfall processes.

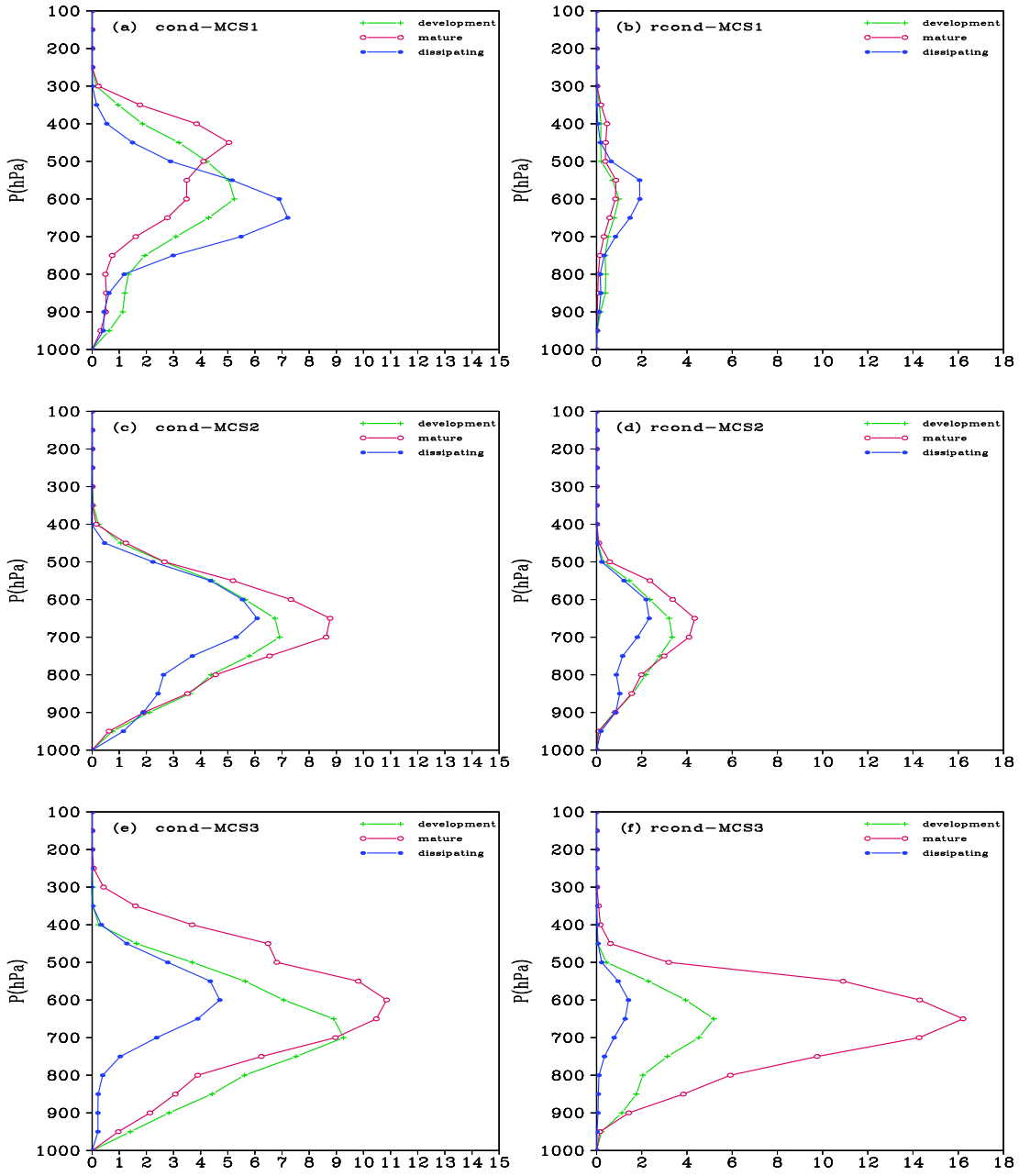

Fig. 5. The average latent heat of cond and rcond (units:10^{13} J/h) (110.33°E to 110.41°E, 18.96°N to 19.06°N).

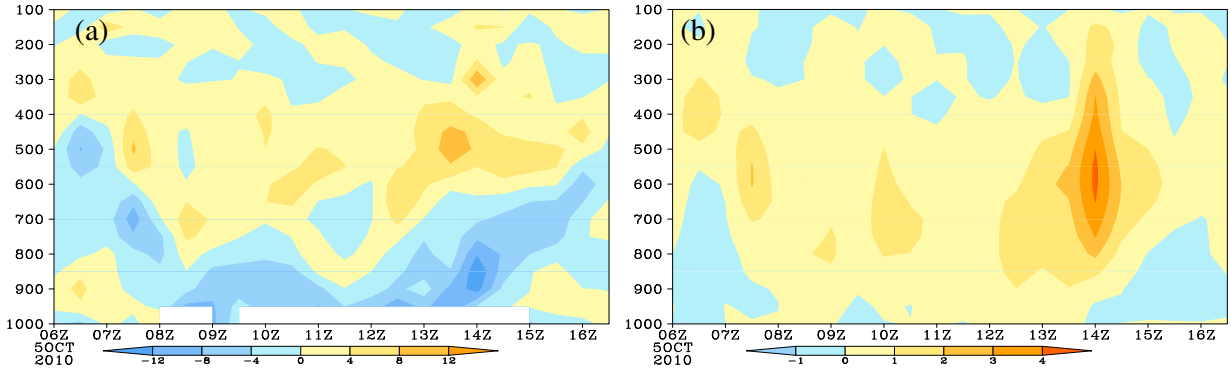

Fig. 6. The average physical quantities of rainstorm (110.33°E to 110.41°E, 18.96°N to 19.06°N). (a) Divergence (unit: 10^{-4} s^{-1}); (b) vertical velocity (unit: m/s).

The total latent heat of MCS1 increases during its short life, while the total latent heat of MCS2 and MCS3 reach a maximum during the mature stage. The difference is mainly caused by the latent heat of water vapor condensed into cloud water and rainwater. The total latent heat released by cond and rcond of MCS1 is smallest during the mature stage. In the middle–low level, the latent heat released by cond and rcond of MCS1 is largest during the dissipating stage. However, it is largest during the mature stage in the middle–high level. The maximums of MCS2 and MCS2 appear below 600 hPa, and the latent heat released by cond and rcond are largest in the mature stage.

The descending motion of the short-lived process (MCS1) are strongest during the mature stage. It caused the smallest latent heat released by water vapor condensed into cloud water and rainwater at the same period. As the air rises, the water vapor condenses. The descending motion is stronger, and the condensation is less. The ascending motion of MCS2 and MCS3 are strongest during the mature stage, and cause the largest latent heat released by the condensation of water vapor. Besides, there are some differences in the change of latent heat released by microphysical processes of MCS2 and MCS3, which are closely related to the drag force of the vertical motion.

Acknowledgments

This study was provided by the National Natural Science Foundation of China under contract No. 41275060, the National Key Basic Research Program of China under contract No. 2014CB953903, the National Natural Science Foundation of China under contract No. 41275145, and the Fundamental Research Funds for the Central Universities under contract No. 13lgjc03.

References

Adams-Selin, Rebecca D., van den Heever, Susan C., Johnson, Richard H., 2013. Sensitivity of bow-echo simulation to microphysical parameterizations. Weather Forecast. 28, 1188–1209.
Brown, J.M., 1979. Mesoscale unsaturated downdraft driven by rainfall evaporation: a numerical study. J. Atmos. Sci. 36, 313–338.
Chang, L.T.-C., Chen, G.T.-J., Cheung, K.K.W., 2008. Mesoscale simulation and moisture budget analyses of a heavy rain event over southern Taiwan in the Meiyu season. Meteorog. Atmos. Phys. 101, 43–63.
Chen, Dudhia, J., 2001. Coupling an advanced land-surface/ hydrology model with the Penn State/NCAR MM5 modeling system: Part I. Model description and implementation. Mon. Weather Rev. 129, 569–585.
Dudhia, J., 1989. Numerical study of convection observed during the winter monsoon experiment using a mesoscale two-dimensional model. J. Atmos. Soc. 46, 3077–3107.
Ebert, E.E., 2008. Fuzzy verification of high-resolution gridded forecasts: a review and proposed framework. Meteorol. Appl. 15, 51–64.
Fu, D.H., Guo, X.L., 2006. A cloud-resolving study on the role of cumulus merger in MCS with heavy precipitation. J. Adv. Atmos. Sci. 23, 857–868.
Fujita, T., 1959. Precipitation and cold-air production in meso-scale thunderstorm systems. J. Meteorol. 16, 454–466.
Gao, S.T., Ping, F., Li, X.F., 2006. Cloud microphysical processes associated with the diurnal variations of tropical convection: a 2D cloud resolving modeling study. Meteorol. Atmos. Phys. 91, 9–16.
Grell, G.A., Devenyi, D., 2002. A generalized approach to parameterizing convection combining ensemble and data assimilation techniques. Geophys. Res. Lett. 29 (14), 38:1–38:4.
Hanssen, A.W., Kuipers, W.J.A., 1965. On the relationship between the frequency of rain and various meteorological parameters. Meded. Verh. 81, 2–15.
Hong, S.-Y., Lim, 2006. The WRF single moment 6-class microphysics scheme(WSM6). J. Kor. Meteorol. Soc. 42, 129–151.
Hou, T.J., Kong, F.Y., Chen, X.L., et al., 2015. Evaluation of radar and automatic weather station data assimilation for a heavy rainfall event in southern China. Adv. Atmos. Sci. 32 (7), 967–978.
Houze Jr., R.A., 1993. Cloud Dynamics. Academic Press (573 pp.).
Huang, Yongjie, Cui, Xiaopeng, 2015. Dominant cloud microphysical processes of a torrential rainfall event in Sichuan, China. Adv. Atmos. Sci. 32 (3), 389–400.
Kim, H.W., Lee, D.K., 2006. An observational study of mesoscale convective systems with heavy rainfall over the Korean Peninsula. Weather Forecast. 21, 125–148.
Lauwaet, D., van Lipzig, N.P.M., De Ridder, K., 2009. The effect of vegetation changes on precipitation and mesoscale convective systems in the Sahel. Clim. Dyn. 33, 521–534.
Li, Xiaofan, Sui, C.-H., Lau, K.-M., 2002. Dominant cloud microphysical processes in a tropical oceanic convective system: a 2D cloud resolving modeling study. Mon. Weather Rev. 130, 2481–2491.
Li, Jiangnan, Wang, Gang, Lin, Wenshi, He, Qihua, Feng, Yerong, Mao, Jiangyu, 2013a. Cloud-scale simulation study of Typhoon Hagupit (2008) Part I: Microphysical processes of the inner core and three-dimensional structure of the latent heat budget. Atmos. Res. 120, 170–180.
Li, Jiangnan, Wang, Gang, Lin, Wenshi, He, Qihua, Feng, Yerong, Mao, Jiangyu, 2013b. Cloud-scale simulation study of Typhoon Hagupit (2008) Part II: Impact of cloud microphysical latent heat processes on typhoon intensity. Atmos. Res. 120, 202–215.
Lim, K.-S., Hong, S.-Y., 2010. Development of an effective double-moment cloud microphysics scheme with progostic cloud condensation nuclei (CCN) for weather and climate models. Mon. Weather Rev. 138, 1587–1612.
Lin, Y.-L., Farley, R.D., Orville, H.D., 1983. Bulk parameterization of the snow field in a cloud model. J. Appl. Meteorol. 22 (6), 1065–1092.
Lin, Hsin-mu, Wang, P.K., Schlesinger, R.E., 2005. Three-dimensional nonhydrostatic simulations of summer thunderstorms in the humid subtropics versus high plains. Atmos. Res. 78, 103–145.
Lou, X.F., Hu, Z.J., Shi, Y.Q., Wang, P.Y., Zhou, X.J., 2003. Numerical simulation of a heavy rainfall case in South China. Adv. Atmos. Sci. 20, 128–138.
Mellor, G.L., Yamada, T., 1982. Development of a turbulence closure model for geophysical fluid problems. Rev. Geophys. Space Phys. 20, 851–875.
Meng, Weiguang, Anyu, Wang, Li, Jiangnan, Fong, Soikun, Hao, I-pan, 2003. Numerical simulation of a mesoscale convective system (MCS) during first rainy season over South China. Acta Meteorol. Sin. 17, 79–92.
Meng, Weiguang, Li, Jiangnan, Wang, Anyu, Fong, Soikun, Ku, Chimeng, Yan, Jinghuay, 2005. Effects of condensation heating and surface fluxes on the development of a South China mesoscale convective system (mcs). J. Trop. Meteorol. 11, 144–153.
Mlawer, E.J., Taubman, S.J., Brown, P.D., Iacono, M.J., Clough, S.A., 1997. Radiative transfer for inhomogeneous atmosphere: RRTM, a validated correlated-k model for the longwave. J. Geophys. Res. 102, 16663–16682.
Molinari, J., Dudek, M., 1992. Parameterization of convective precipitation in mesoscale numerical models: a critical review. Mon. Weather Rev. 120, 326–344.
Monin, A.S., Obukhov, A.M., 1954. Basic laws of turbulent mixing in the surface of the atmosphere. Tr. Akad. Nauk SSSR Geophiz. Inst. 151, 163–187.
Morrison, H., Thompson, G., Tatarskii, V., 2009. Impact of cloud microphysics on the development of trailing stratiform precipitation in a simulated squall line: comparison of one-and two-moment schemes. Mon. Weather Rev. 137 (3), 991–1007.
Park, S.G., Lee, D.K., 2009. Retrieval of high-resolution wind fields over southern Korean Peninsula using Doppler weather radar network. Weather Forecast. 24, 87–103.
Parker, M.D., 2007. Simulated convective lines with parallel stratiform precipitation: Part I. An Archetype for Convection in Along-Line Shear. J. Atmos. Sci. 64, 267–288.
Peters, John M., Schumacher, Russ S., 2015. The simulated structure and evolution of a quasi-idealized warm-season convective system with a training convective line. J. Atmos. Sci. 72, 1987–2010.
Roberts, N., Lean, H., 2008. Scale-selective verification of rainfall accumulations from high-resolution forecasts of convective events. Mon. Weather Rev. 136, 78–97.
Sun, Tingkai, Tan, Zhemin, 2001. Numerical simulation study for the structure and evolution of tropical squall line. Adv. Atmos. Sci. 18 (1), 117–138.
Takuya, Kawabata, Iwai, Hironori, Seko, Hiromu, Shoji, Yoshinori, Saito, Kazuo, Ishii, Shoken, Mizutani, Kohei, 2014. Cloud-resolving 4D-Var assimilation of Doppler wind Lidar data on a meso-gamma-scale convective system. Mon. Weather Rev. 142, 4484–4498.
Tao, Yue, Qi, Yanbin, Hong, Yanchao, 2012. Numerical study of the influence of the latent heat on the mesoscale convective system and precipitation during a torrential rain event in North China. Acta Meteorol. Sin. 70 (1), 50–64.
Wang, Xiaofang, Cui, Chunguang, 2011. A number of advances of the research on heavy rain mesoscale convective systems. Torrential Rain Disasters 30 (2), 97–106.
Wang, Xiaofang, Cui, Chunguang, 2012. Analysis of the linear mesoscale convective systems during the Meiyu period in the middle and lower reaches of the Yangtze River. Part I: Organization mode features. Acta Meteorol. Sin. 70 (5), 909–923.
Wang, P.Y., Yang, J., 2003. Observation and numerical simulation of cloud physical processes associated with torrential rain of the Meiyu front. Adv. Atmos. Sci. 20, 77–96.
Wang, Donghai, Li, Xiaofan, Tao, Wei-Kuo, Liu, Ying, Zhou, Haiguang, 2009. Torrential rainfall processes associated with a landfall of severe tropical storm Bilis (2006): a two-dimensional cloud-resolving modeling study. Atmos. Res. 91, 94–104.
Wang, Xiaofang, Cui, Chunguang, Cui, Wenjun, Shi, Yan, 2014. Modes of mesoscale convective system organization during Meiyu season over the Yangtze River basin. J. Meteorol. Res. 28 (1), 111–126.
Xu, W.H., Ni, Y.Q., Wang, X.K., Qiu, X.X., Bao, X.H., Jin, W.Y., 2011. A study of structure and mechanism of a meso-beta-scale convective vortex and associated heavy rainfall in the Dabie Mountain area Part I: Diagnostic analysis of the structure. Adv. Atmos. Sci. 28 (5), 1159–1176.
Zhao, Yuchun, 2015. A study on the heavy-rain-producing mesoscale convective system associated with diurnal variation of radiation and topography in the eastern slope of the western Sichuan plateau. Meteorog. Atmos. Phys. 127, 123–146.
Zheng, Linlin, Sun, Jianhua, Zhang, Xianlong, et al., 2013. Organizational modes of mesoscale convective systems over central East China. Weather Forecast. 28 (5), 1081–1098.